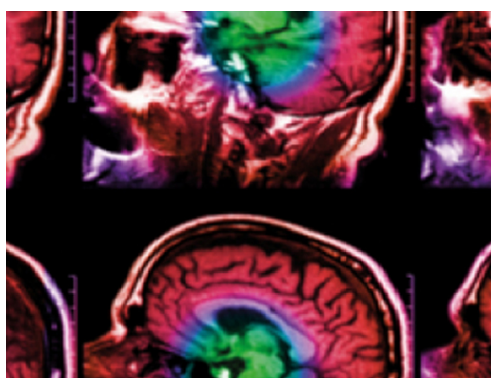


PAPER

## Polaroid-PET: a PET scanner with detectors fitted with Polaroid for filtering unpolarized optical photons—a Monte Carlo simulation study

To cite this article: Amirhossein Sanaat *et al* 2020 *Phys. Med. Biol.* **65** 235044

View the [article online](#) for updates and enhancements.



**IPEM | IOP**

Series in Physics and Engineering in Medicine and Biology

Your publishing choice in medical physics,  
biomedical engineering and related subjects.

Start exploring the collection—download the  
first chapter of every title for free.



## PAPER

# Polaroid-PET: a PET scanner with detectors fitted with Polaroid for filtering unpolarized optical photons—a Monte Carlo simulation study

RECEIVED  
20 April 2020REVISED  
20 July 2020ACCEPTED FOR PUBLICATION  
12 August 2020PUBLISHED  
30 November 2020Amirhossein Sanaat<sup>1</sup> , Aydin Ashrafi-Belgabad<sup>2</sup> and Habib Zaidi<sup>1,3,4,5,\*</sup> <sup>1</sup> Division of Nuclear Medicine and Molecular Imaging, Geneva University Hospital, Geneva 1211, Switzerland<sup>2</sup> Physics and Energy Engineering Department, Amirkabir University of Technology, Tehran, Iran<sup>3</sup> Geneva University Neurocenter, Geneva University, Geneva 1205, Switzerland<sup>4</sup> Department of Nuclear Medicine and Molecular Imaging, University of Groningen, University Medical Center Groningen, Groningen, The Netherlands<sup>5</sup> Department of Nuclear Medicine, University of Southern Denmark, DK-500, Odense, Denmark

\* Author to whom any correspondence should be addressed.

E-mail: [habib.zaidi@hcuge.ch](mailto:habib.zaidi@hcuge.ch)**Keywords:** PET, instrumentation, detectors, Polaroids, spatial resolution

## Abstract

We propose and evaluate the performance of an improved preclinical positron emission tomography (PET) scanner design, referred to as Polaroid-PET, consisting of a detector equipped with a layer of horizontal Polaroid to filter scintillation photons with vertical polarization. This makes it possible to improve the spatial resolution of PET scanners based on monolithic crystals. First, a detector module based on a lutetium-yttrium orthosilicate monolithic crystal with 10 mm thickness and silicon photomultipliers (SiPMs) was implemented in the GEANT4 Monte Carlo toolkit. Subsequently, a layer of Polaroid was inserted between the crystal and the SiPMs. Two preclinical PET scanners based on ten detector modules with and without Polaroid were simulated. The performance of the proposed detector modules and corresponding PET scanner for the two configurations (with and without Polaroid) was assessed using standard performance parameters, including spatial resolution, sensitivity, optical photon ratio detected for positioning, and image quality. The detector module fitted with Polaroid led to higher spatial resolution (1.05 mm FWHM) in comparison with a detector without Polaroid (1.30 mm FWHM) for a point source located at the center of the detector module. From 100% of optical photons produced in the scintillator crystal, 65% and 66% were used for positioning in the detectors without and with Polaroid, respectively. Polaroid-PET resulted in higher axial spatial resolution (0.83 mm FWHM) compared to the scanner without Polaroid (1.01 mm FWHM) for a point source at the center of the field of view (CFOV). The absolute sensitivity at the CFOV was 4.37% and 4.31% for regular and Polaroid-PET, respectively. Planar images of a grid phantom demonstrated the potential of the detector with a Polaroid in distinguishing point sources located at close distances. Our results indicated that Polaroid-PET may improve spatial resolution by filtering the reflected optical photons according to their polarization state, while retaining the high sensitivity expected with monolithic crystal detector blocks.

## 1. Introduction

Positron emission tomography (PET) is a powerful molecular imaging modality widely used in clinical diagnosis, staging and restaging, monitoring of treatment response, and radiation treatment planning. Despite the tremendous specificity of the information it provides at the molecular and cellular level, in addition to being a quantitative imaging modality by nature, PET still suffers from relatively poor spatial resolution and moderate sensitivity. The former is commonly in the range of 3–6 mm in clinical scanners

(Moses 2011, van Sluis *et al* 2019) and 0.8 to 1.3 mm in preclinical scanners (Zaidi 2014, Zaidi and Karakatsanis 2017). Despite recent advances in PET instrumentation, the sensitivity of clinical PET scanners is still limited owing to the limited axial field of view (FOV). This has motivated the emergence of the concept of total-body PET (Zhang *et al* 2020) and a number of approaches to reduce the cost of this design (Zein *et al* 2020, Surti *et al* 2020). The limitations of current-generation PET scanners in terms of spatial resolution and sensitivity are challenging the detectability and reliable characterization of small structures and lesions in human/rodent imaging.

Despite the impressive progress in PET instrumentation witnessed since the invention of this imaging modality in the 1970s, there are still plenty of opportunities and high-tech approaches that can improve further the performance of PET scanners (Jones and Townsend 2017, Berg and Cherry 2018). One of the most challenging problems in an ideal PET scanner is the inherent trade-off that exists between the power of the spatial resolution and the system sensitivity (Lewellen 2010). This trade-off is due to the use of thick and wide pixel-size crystals, which leads to good sensitivity but bad spatial resolution caused by parallax error (Godinez *et al* 2012). A number of strategies have been devised to mitigate this issue by using depth-of-interaction (DOI) information in the calculation of the interaction position (Moses 2001). Furthermore, the reduction of crystal pixel size (in pixelated modules) and crystal thickness (in monolithic modules) has a direct correlation with the enhancement of spatial resolution. However, this is achieved at the expense of a degradation of the scanner sensitivity and the crystal identification accuracy in pixelated crystals (owing to inter-crystal penetration) and an increase of optical photon inter-reflections in monolithic crystals (Miyaoka and Lewellen 2000, Ota *et al* 2016). The above-mentioned challenges lead to a trade-off between spatial resolution and energy/timing resolution (Cherry *et al* 1997, Lewellen 2010). Recently, monolithic crystals have been employed to achieve high spatial resolution thanks to their ability to support the extraction of DOI features, as well as methodologies for better discriminating deposited energy and timing information (Sanaat and Zaidi 2019, 2020, Sanaat *et al* 2019b). Monolithic detector blocks also contain no zero detection zones, unlike pixelated crystals, thus offering a larger volume to interact with the emitted annihilation photons and collect the resulting optical photon signal generated as a result of the photon interactions (Maas *et al* 2009). However, these types of detectors need a complicated calibration process and concern for choosing the optimized thickness to reserve the sensitivity and spatial resolution at the same time (Vinke *et al* 2010, Seifert *et al* 2013, Pierce *et al* 2018).

A number of innovative strategies have been devised to improve the overall performance of PET detector modules, including the development of novel scintillation crystals (Ghabrial *et al* 2018). Ramirez *et al* showed that the spatial and energy resolutions can be improved in human and animal PET scanners using polymer mirror film patterns placed between the scintillator segments (in pixelated crystals) as reflector and photomultiplier-quadrant-sharing technology (Ramirez *et al* 2008). Sabet *et al* proposed a detector module combining the advantageous characteristics of pixelated and monolithic crystals (Sabet *et al* 2012). They used a technique called laser-induced optical barriers (LIOB) to create some defects inside the crystal that had a different refractive index from the main crystal bulk (Blackberg *et al* 2018), and used these optical barriers as a reflector to convert monolithic crystals to pseudo-pixelated ones. Sanaat *et al* reported on a new technique for deflecting the trajectory of scintillation photons passing through a scintillator (Sanaat *et al* 2019a). The proposed method consists of a reflective belt created from millions of optical barrier points covering the surroundings of the crystal, created by the LIOB method. A monolithic crystal with a belt of reflectors created by laser engraving can lead to better spatial resolution and sensitivity. More recent work suggested a high-resolution depth encoding detector using a prismatoid light guide array that employs right triangular prisms to increase inter-crystal light sharing, thus enhancing both the DOI resolution and crystal identification (Labella *et al* 2020). The detector module is capable of achieving a uniform spatial resolution, a high sensitivity, and fine timing and energy resolution.

Light rays are electromagnetic waves produced as a result of the scintillation process. They have different orientation distributions related to the directionality of the electric and magnetic fields, called polarization. Polaroid is a type of synthetic plastic sheet used as a polarizer or polarizing filter (Collett 2005). Polarizers improve image quality and contrast by removing glare, haze, and reflections (Iqbal 2011). Two types of polarizers are used in optical systems: linear polarizers and circular polarizers. Linear polarizations are more effective and less expensive than circular ones. In this work, we focus on this type of Polaroid. Implementing polarization control can be useful in a variety of imaging applications. Polarization is an important property of light that affects even optical systems that do not explicitly measure it. Polarizers are placed over a light source, a lens, or both, to eliminate glare from light scattering, increase contrast, and eliminate hot spots from reflective objects (Peatross and Ware 2017). Polarization can be caused by a range of phenomena, such as scattering, reflection, and transmission through media interfaces, or may be altered relative to the initial state (Andreou and Kalayjian 2002, Ikeuchi 2014). In reality, most scintillation photons are unpolarized light

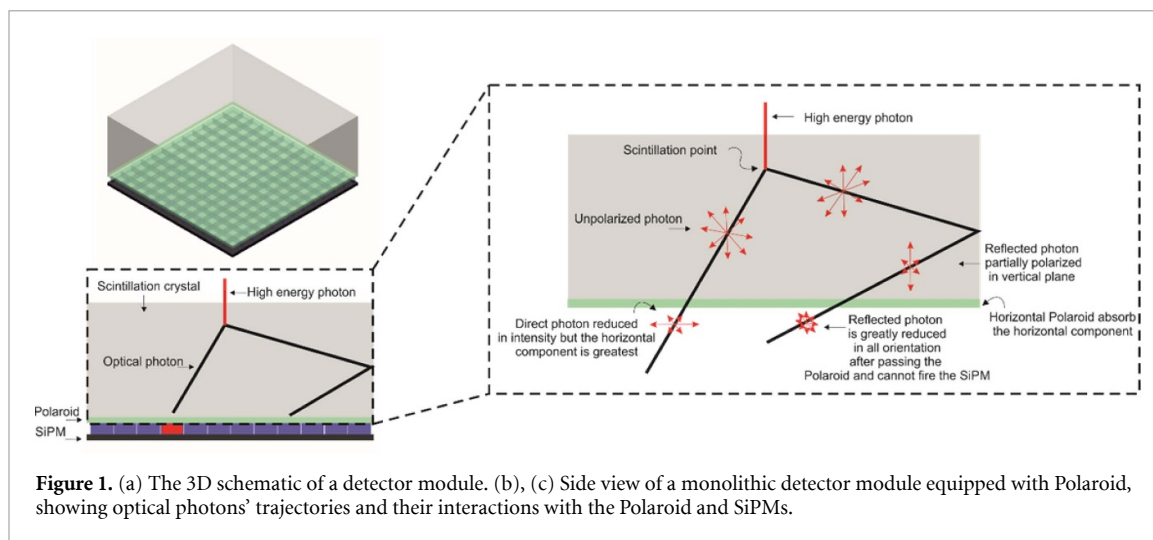


**Figure 1.** (a) The 3D schematic of a detector module. (b), (c) Side view of a monolithic detector module equipped with Polaroid, showing optical photons' trajectories and their interactions with the Polaroid and SiPMs.

because of the stochastic nature of the scintillation process. Other phenomena, such as internal reflections and variation of materials, change the polarization of light (Können 1985).

Optical photons have two states inside the crystal. First, the unpolarized state, where optical photons are unpolarized right after the scintillation and are allowed to pass through a horizontal Polaroid and reach the silicon photomultipliers (SiPMs). When they pass through the horizontal Polaroid, they will have a horizontal polarization. Second, the reflection state, where unpolarized optical photons are reflected by surrounding reflectors and will have a vertical polarization, which prevents them from passing through the horizontal Polaroid to reach the SiPMs (Andreou and Kalayjian 2002, Pedrotti *et al* 2017).

In this work, we introduce the concept of Polaroid-PET and simulate its performance in a preclinical PET scanner geometry equipped with a single-ended readout and depth-encoding detector module that uses a layer of Polaroid located between the scintillator and SiPMs. Our designed detector is easy to use and cost-effective to implement, by adding a thin layer of Polaroid between the SiPMs and scintillator. Our method can be easily extended to clinical PET scanners, where we expect to obtain even better results than in preclinical PET scanners.

## 2. Materials and methods

### 2.1. Geometrical preclinical PET configurations

The main goal of this study is to present a novel detector configuration for a preclinical PET scanner aiming at attaining improved trade-off between sensitivity and spatial resolution. High spatial resolution implies that the fine details of an image can be distinguished, defining more specifically how close two point/line sources can be to each other and still be visually distinguishable. The motivation behind the proposed design concept lies in the use of monolithic scintillation crystals along with SiPMs and a layer of Polaroid located between the crystal and SiPMs. The proposed new PET detector module was then implemented into a preclinical PET scanner platform. The detector based on monolithic scintillators, having relatively higher detection efficiency, is employed to maintain/boost the absolute sensitivity, whereas the Polaroid is exploited to retain/enhance the spatial resolution of the detector. To assess the role of Polaroid, two preclinical PET configurations were modeled using ten detector blocks with and without Polaroid. The main reason behind the choice of ten detector blocks in these two configurations is to match the geometry of an existing PET scanner to enable further experimental validation in a similar geometry (Sajedi *et al* 2019, Amirrashedi *et al* 2019). Figure 1 illustrates the schematic of the detector in the presence of Polaroid from different angles. Annihilation photons (511 keV) enter the crystal, causing the occurrence of the scintillation process. Then optical light is emitted isotropically in random directions. Some photons go straight to the photodetector (SiPMs), whereas others may hit the walls and reflect multiple times. These multiple reflections of optical photons lead to inaccurate localization inside the crystal, thus degrading the PET scanner's spatial resolution, and consequently causing glaring and reduced image quality. To prevent this phenomenon, a linear polarizer can be used to eliminate unwanted light with different polarization states regarded as scattering or reflection.

#### 2.1.1. Preclinical PET detector block

To test the effectiveness of the proposed concept, we evaluated the performance of a preclinical PET scanner's detector blocks with and without Polaroid using realistic Monte Carlo simulations. In the regular

configuration, we simulated a detector block consisting of a monolithic lutetium-yttrium orthosilicate (LYSO) scintillator with a  $50.2 \times 50.2 \text{ mm}^2$  entrance area and 10 mm crystal thickness, coupled to a SiPM array with  $12 \times 12$  size and 4.2 mm pixel pitch (Sensl Array C-30 035-144P-PCB). A barium sulfate ( $\text{BaSO}_4$ ) sheet with a thickness of 0.1 mm was used to warp the crystal as the crystal reflector. For optical coupling in detector modules equipped with Polaroid, two glue layers, each of 0.05 mm thickness, were employed between the crystal and the Polaroid and between the Polaroid and the SiPMs. Conversely, in the regular detector without Polaroid, only one layer of 0.05 mm of glue was used between the crystal and the SiPMs. The presence of a Polaroid film layer and an additional glue layer were the only differences between the Polaroid-PET and regular PET configuration.

### 2.1.2. Preclinical PET scanner configuration

To assess and compare the performance of the proposed detector module in a preclinical scanner, two detector modules with and without Polaroid were considered for simulation.

## 2.2. Monte Carlo simulations

Monte Carlo simulations of nuclear imaging instrumentation require accurate modeling of the trajectory of optical photons produced by the scintillation process, considering all physical processes occurring within the scintillator, optical interactions (e.g. reflection, refraction, and absorption) and the outcome of electronic circuits, which convert photon intensity into electrical signals. To accomplish the previously stated goal, Monte Carlo simulations of a single detector module with and without the Polaroid were performed for preclinical PET models (regular and Polaroid-PET) using the GEANT4 code (version 4.10.2) (Agostinelli *et al* 2003). Moreover, since optical transport is one of the important aspects of this study, a realistic simulation model was implemented.

To track scintillation photons and produce electrons, the required GEANT4 libraries for optical photon interaction (G4OpAbsorption, G4OpRayleigh, G4MultipleScattering, G4OpScintillation, G4OpBoundaryProcess, G4OpScintillation, G4OpAbsorption, and G4MultipleScattering) and electron interactions (G4eIonisation and G4eBremsstrahlung) were added to the simulation physics list. Additionally, several libraries for adding ionization photons into the simulation process were considered (G4LowEnergyRayleigh, G4LowEnergyCompton, and G4LowEnergyPhoto-Electric) (Allison *et al* 2006, 2016). Polarization was taken into account using the appropriate class of G4LivermorePolarizedComptonModel (Depaola, 2003). The interaction of optical photons based on Snell's law at the boundaries of two different materials was precisely modeled using the well-established UNIFIED model in GEANT4 (Nayar *et al* 1991).

In this simulation workflow, the reflection probability was considered to be 97%, which means most of the photons are reflected on the surface of the reflector and only 3% are absorbed based on the employed 'Paint' model (van der Laan *et al* 2010). Similarly, for surfaces interfacing the crystal–glue, glue–Polaroid, Polaroid–glue, and glue–SiPM layers, the 'Ground' model was utilized (Levin and Moisan 1996, van der Laan *et al* 2010). Refractive indices of 1.82, 1.42, 1.91, and 1.6 were used for crystal, glue, polarized film, and SiPMs, respectively. It should be mentioned that in surface models of GEANT4, for each photon that touches the boundary of two different materials with various refractive indices there is a unique probability for reflection or refraction. In this simulation, the refractive index of the LYSO was set to 1.82 and a light yield of 25 000 optical photons per MeV was considered, according to the characteristics of the LYSO crystal based on the datasheet provided by the manufacturer. Furthermore, the reflectivity and photon detection efficiency of the SiPMs were set to 20% and 23%, respectively. For event positioning calculation and energy discrimination, the light intensity values of the 144 SiPM pixels were added up and only events in the full energy peak were used.

## 2.3. Positioning algorithm

The extraction of the position of each event in the monolithic crystal was estimated based on the correlated signal enhancement (CSE) positioning algorithm using an in-house software developed in C++ computer code. More specifically, in this method we record and calculate the polarization and the number of scintillation photons absorbed by each of the 144 SiPM pixels ( $12 \text{ rows} \times 12 \text{ columns}$ ). In each scintillation process, we record and sum the number of polarized scintillation photons reaching the pixels in each row and column separately. Then simple 1D center of mass (COM) is applied independently for each direction ( $X$  and  $Y$  directions of the SiPM array) to estimate the position of each scintillation point inside the crystal (Flower 2012, Teimourian Fard and Shamsaei Zafarghandi 2019). To attain an improved spatial resolution and linearity, a nonlinear correction function was applied on the column and row summation values. The formulas used to estimate  $X$  and  $Y$  are as follows:

$$X = \frac{\sum_j x_{C_j} W_f(C\_nor_j) C_j (\geq S_{min})}{\sum_j C_j (\geq S_{min})}, C_j = \sum_i S_{j,i}, C\_nor_j = \frac{\sum_i S_{j,i}}{\sum_j \sum_i S_{j,i}} \quad (1)$$

$$Y = \frac{\sum_i y_{R_i} W_f(R\_nor_i) R_i (\geq S_{min})}{\sum_i R_i (\geq S_{min})}, R_i = \sum_j S_{j,i}, R\_nor_i = \frac{\sum_j S_{j,i}}{\sum_j \sum_i S_{j,i}} \quad (2)$$

where  $i$  and  $j$  denote the rows and columns (varying from 1 to 12), respectively, and  $S_{ij}$  is the number of events recorded by SiPMs in the  $i$ th row and  $j$ th column.  $x_{C_j}$  and  $y_{R_i}$  are the coordinates of the center of the  $i$ th row and  $j$ th column defined based on the SiPM geometry (a predefined lookup table contains the coordinates, including the centers of rows and columns). A Gaussian correction function denoted  $W_f$  that modifies the signal (here the counts/pixels are linked with the signal's magnitude) of each column and row (Zeraatkar *et al* 2017). The function was optimized and evaluated for the present detector in our previous studies (Zeraatkar *et al* 2017).

$$W_f(x) = \exp \left[ -\frac{(x - 0.3)^2}{2(0.5)^2} \right]. \quad (3)$$

$W_f$  applies a weighting factor that optimizes weak and strong signals regarding the column (row) summation. Weak signals lead to a poor signal-to-noise ratio (SNR), whereas strong signals do not contain valuable information about the interaction position. A threshold level of 2% (representing  $S_{min}$  in equations (1) and (2)) was applied in the same manner as the conventional COM technique in the considered PET scanner (Jansen and Binnie 1996, Galasso *et al* 2016). This experimentally determined threshold led to the criterion adopted in the simulation with respect to accepting or rejecting optical photons. In our positioning algorithm, we assigned zero to the pixels of the SiPMs farthest from the hottest pixel (pixels at a distance equal to or higher than half of the detector's width (25.1 mm) from the hottest pixel). Second, we assigned zero to pixels with counts that were less than 2% of the scintillation ratio.

## 2.4. Image reconstruction

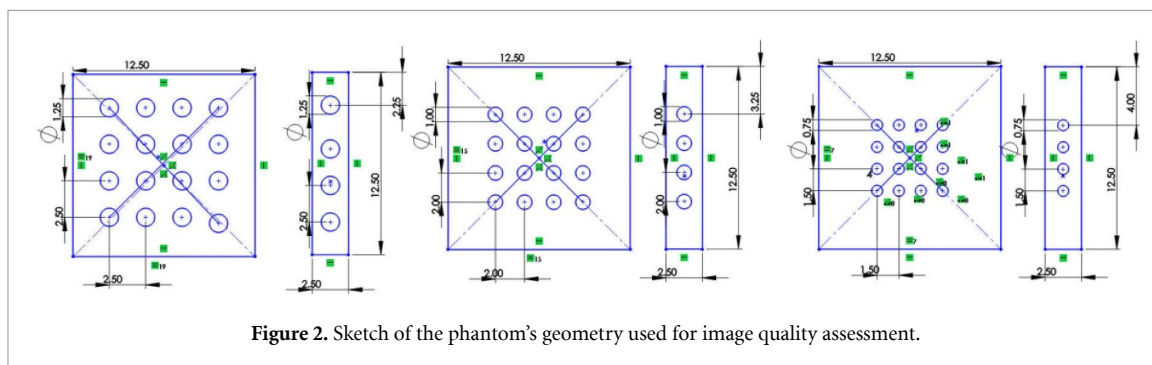
Scintillation position extraction of each event in the monolithic crystal was estimated based on the CSE positioning algorithm using an in-house software developed in C++ computer code. Based on our experimental setup, the energy and time window of the simulated scanner were set at 150–650 keV and 4 ns, respectively. Then, for each event, the optical photons absorbed by the SiPMs' pixels were stored in a root file (Brun and Rademakers 1997) and labeled with pixel numbers and polarization vectors. The origin of scintillation events was estimated for each detector block by applying the CSE algorithm to the scintillation photon distribution. A line was connected to two scintillation events as a line of response (LOR). The LORs were stored and labeled with their corresponding angulation and distance from the central axes of the scanner. The single-slice rebinning algorithm was applied to rebin the LORs from oblique planes to direct plane. The stored LORs were projected in the sinogram space, followed by image reconstruction using a 2D filtered back projection algorithm implemented within the STIR package (Thielemans *et al* 2012). 2D reconstruction was adopted to stay consistent with the current version of the software used on the Xtrim-PET scanner modeled in this work (Sajedi *et al* 2019, Amirrashedi *et al* 2019). The energy of each annihilation photon was estimated by summing up all the optical photons that reached a SiPM's pixel after applying the positioning threshold and Polaroid filtration (summation of 65% of all the produced optical photons). Analytical modeling was adopted to recover the missing energy (around 35% of energy was missed because of the positioning threshold and Polaroid).

## 2.5. Validation and performance evaluation

The regular scanner model simulated using GEANT4 and the image reconstruction algorithm were validated (Sanaat *et al* 2019b, 2020) against comparison with the experimental results acquired on a prototype preclinical PET scanner designed and fabricated in our lab (Sajedi *et al* 2019, Amirrashedi *et al* 2019). Experimental validation of the proposed Polaroid-PET was not possible at this stage since the scanner was not fabricated yet. Table 1 summarizes the technical specifications of the prototype detector and scanner implemented in Monte Carlo simulations. The performance of the proposed preclinical PET model was assessed using the NEMA NU4-2008 standard (National Electrical Manufacturers Association 2008). Owing to the lengthy computational time of Monte Carlo simulations when evaluating the count rate performance in previous studies, we focused mostly on the assessment of key performance parameters, including spatial resolution, sensitivity and optical photon detection ratio between the regular and Polaroid-PET models.

**Table 1.** Physical characteristics and dimensions of the preclinical PET scanner used for the validation of GEANT4 Monte Carlo simulations.

| Parameter                    | Value                                |
|------------------------------|--------------------------------------|
| Number of block rings        | 1                                    |
| Detector blocks per ring     | 10                                   |
| Scintillator material        | LYSO                                 |
| Crystals per block           | $24 \times 24 = 576$                 |
| Axial FOV                    | 50 mm                                |
| Transaxial FOV               | 100 mm                               |
| Number of image planes       | 109                                  |
| Coincidence time window      | 4.0 ns                               |
| Energy window                | 150–650 keV                          |
| Energy resolution            | 11.7%                                |
| Detector block entrance area | $50 \times 50 \text{ mm}^2$          |
| Crystal size (thickness)     | $2 \times 2 \times 10 \text{ mm}^3$  |
| Detector ring diameter       | 168 mm                               |
| Photodetector                | SiPM                                 |
| Array size                   | $12 \times 12$                       |
| Pixel pitch                  | 4.2 mm                               |
| Light guide size             | $50 \times 50 \times 3 \text{ mm}^3$ |
| Reflector material           | BaSO <sub>4</sub>                    |
| Thickness                    | 0.1 mm                               |

**Figure 2.** Sketch of the phantom's geometry used for image quality assessment.

### 2.5.1. Spatial resolution

The spatial resolution for a single detector module and a whole PET scanner was evaluated separately. For a single detector module, this parameter was calculated by placing a  $^{22}\text{Na}$  point source (1 mm diameter and 148 kBq activity) fixed inside a 1 cm<sup>3</sup> block of acrylic at a distance equal to the radius of the gantry (84 mm) and then moving it with a 5 mm step size on a surface parallel to the detector block in the X and Y directions. The spatial resolution was obtained by calculating the full width at half maximum (FWHM) of a Gaussian function fitted on the intensity profile of the point source image. Estimation of the spatial resolution for the whole PET scanner was based on the NEMA NU 4–2008 standard. The spatial resolution of the regular and Polaroid-PET was estimated using the above-mentioned point source, located at various radial positions along the central axis of the PET scanner. The point source was moved from the center to edge of the FOV in the radial and axial directions with a 5 mm step size corresponding to six positions in each direction (0, 5, 10, 15, 20, and 25 mm) to survey the impact of parallax error on the spatial resolution.

### 2.5.2. Sensitivity

The absolute sensitivity of the regular and Polaroid-PET scanner was examined along the axial FOV through 11 scans of a  $^{22}\text{Na}$  point source (180 kBq) for an acquisition time of 10 min. The point source was moved with a step size of 5 mm from one side of the axial FOV to the other. Based on the NEMA NU4 protocol, the activity of the point source was chosen relatively low to guarantee that the random rate would be lower than 5% and the single event counting losses would be less than 1% of the true coincidence event rate.

### 2.5.3. Image quality

Since the tracking of optical photons is very time-consuming, simulation of a full PET scanner geometry was impractical owing to limited computational power. Hence, we did not include image quality assessment using the NEMA NU4–2008 phantom. Instead, we assessed performance-related metrics for a single detector module through the simulation of a grid of sources consisting of three  $4 \times 4$  arrays of spheres filled

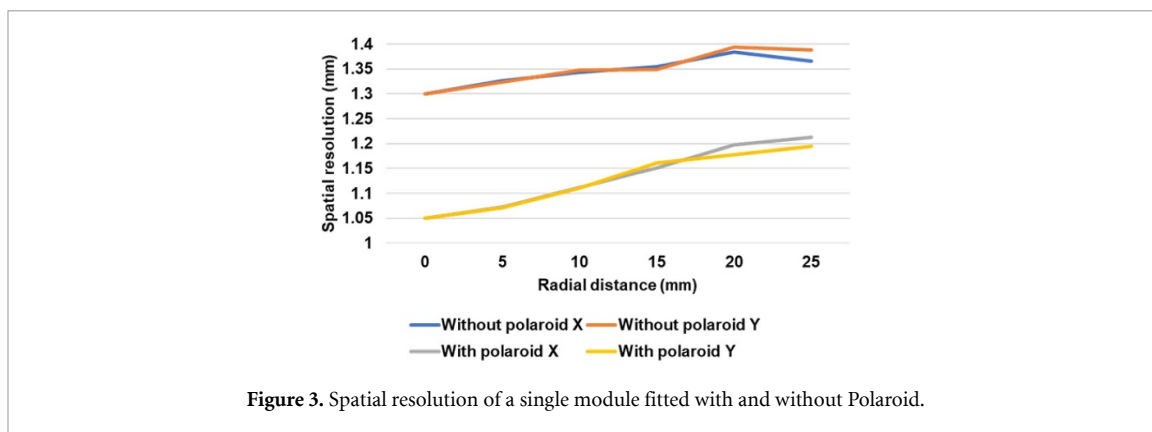


Figure 3. Spatial resolution of a single module fitted with and without Polaroid.

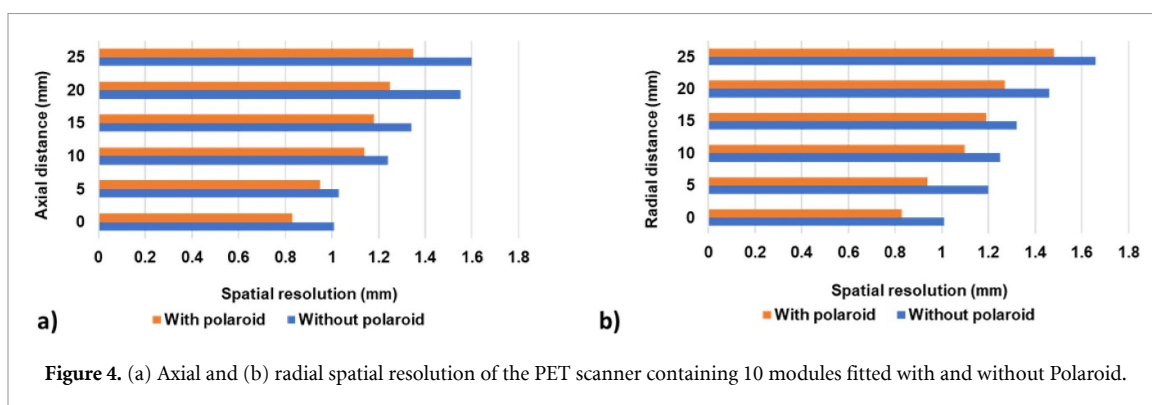


Figure 4. (a) Axial and (b) radial spatial resolution of the PET scanner containing 10 modules fitted with and without Polaroid.

with  $^{18}\text{F}$  embedded in a water-filled tank (figure 2). The diameters of the spheres were 0.75, 1.0, and 1.25 mm (corresponding center-to-center distances were 1.5, 2.0, and 2.5 mm).

### 3. Results

#### 3.1. Validation

The estimated spatial resolution and sensitivity of the regular preclinical PET scanner simulated using the GEANT4 simulation toolkit revealed good agreement with the experimental measurements performed on the Xtrim small-animal PET scanner. The discrepancy between the simulated and measured spatial resolution at the center of FOV (CFOV) did not exceed 5% error, while the error on the absolute sensitivity reached a maximum of 8%. The details of the validation procedure are provided in Sanaat *et al* (2019b).

#### 3.2. Quantitative analysis

The spatial resolution in the X and Y directions estimated for a single PET detector module with and without Polaroid are presented in figure 3. Although the variation of the spatial resolution with distance in the X and Y direction is small, the difference between the detector with and without the Polaroid is remarkable for a preclinical scanner with near sub-millimetric spatial resolution at the CFOV.

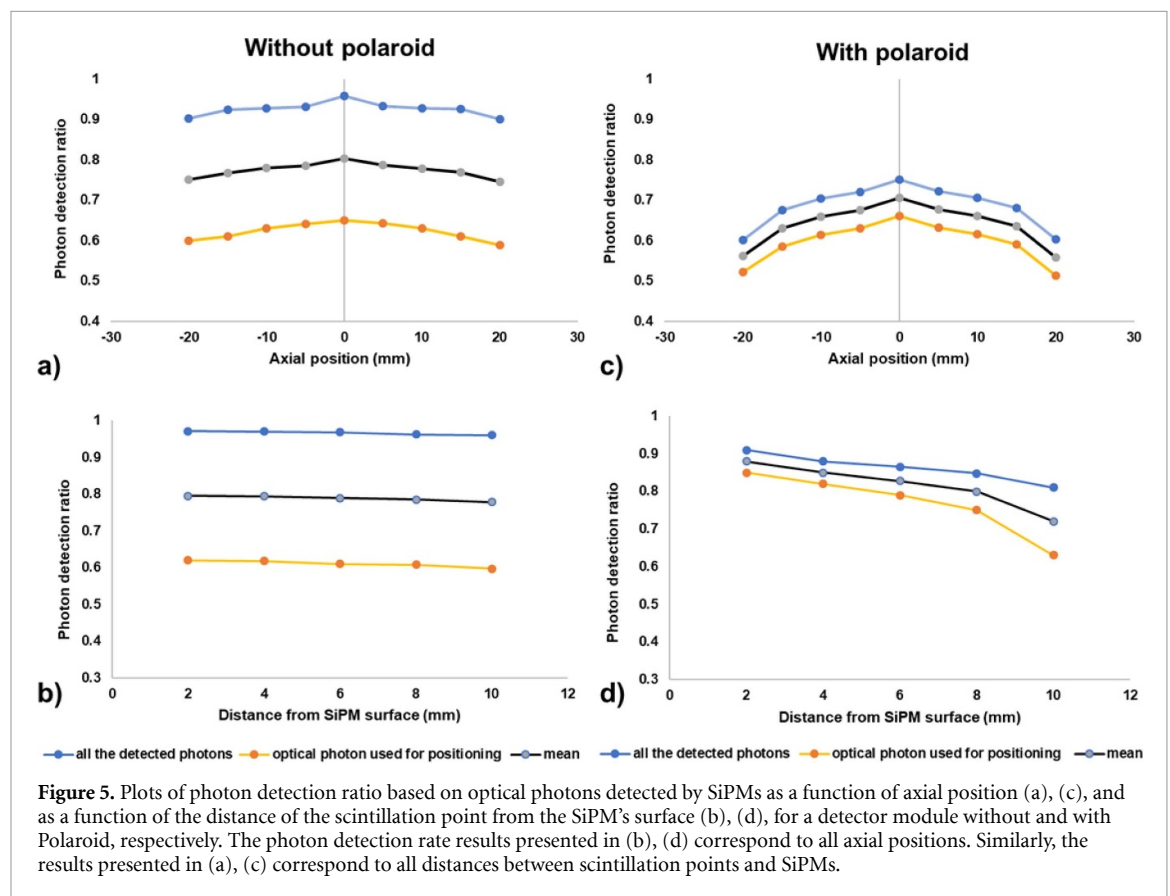
Based on the NEMA NU-4 standard, the spatial resolution of the full PET scanner (consisting of ten detector modules) with and without the Polaroid should be measured at the center and at 1/4 the axial FOV from the center distance. In this work, additional measurements were performed along the axial and radial directions with a step size of 5 mm (figure 4). The axial and radial spatial resolution measured without the Polaroid varied between 1.01 mm and 1.6 mm (FWHM), while Polaroid-PET led to axial spatial resolution varying between 0.83 mm and 1.35 mm FWHM. The results indicate a submillimeter axial and radial spatial resolution for Polaroid-PET for axial and radial distances equal to or smaller than 5 mm.

Table 2 summarizes the absolute sensitivity of PET models with and without the Polaroid, respectively. The sensitivity was measured across the axial FOV using the default energy window of 150–650 keV. The results indicate that the sensitivity stays relatively constant when using the Polaroid.

Figure 5 shows plots of the ratio of the mean number of scintillation photons detected by the SiPMs used to calculate the event position to the total number of scintillation photons detected by all the SiPMs' pixels in one module with and without the Polaroid as a function of the interaction point distance from the SiPMs' surface and the axial position of the event. From all the optical photons produced in the monolithic crystal

**Table 2.** Absolute sensitivity measured at different distances from the center of the FOV along the Z-axis for PET models with and without the Polaroid.

| Distance (mm) | Polaroid-PET $\pm$ STD (%) | Regular-PET $\pm$ STD (%) | P-value            |
|---------------|----------------------------|---------------------------|--------------------|
| -25           | $2.68 \pm 0.03$            | $2.65 \pm 0.07$           | <0.05              |
| -20           | $2.97 \pm 0.07$            | $3.04 \pm 0.03$           | <0.05              |
| -15           | $3.31 \pm 0.1$             | $3.36 \pm 0.08$           | 0.052 <sup>a</sup> |
| -10           | $3.58 \pm 0.07$            | $3.55 \pm 0.06$           | <0.05              |
| -5            | $3.92 \pm 0.09$            | $4.02 \pm 0.07$           | <0.02              |
| 0             | $4.31 \pm 0.08$            | $4.37 \pm 0.04$           | <0.05              |
| 5             | $3.96 \pm 0.09$            | $4.02 \pm 0.06$           | <0.05              |
| 10            | $3.56 \pm 0.07$            | $3.54 \pm 0.1$            | <0.05              |
| 15            | $3.32 \pm 0.08$            | $3.34 \pm 0.07$           | <0.05              |
| 20            | $2.97 \pm 0.06$            | $3.05 \pm 0.03$           | <0.05              |
| 25            | $2.67 \pm 0.07$            | $2.64 \pm 0.07$           | <0.05              |

<sup>a</sup>No proof of statistical significance**Figure 5.** Plots of photon detection ratio based on optical photons detected by SiPMs as a function of axial position (a), (c), and as a function of the distance of the scintillation point from the SiPM's surface (b), (d), for a detector module without and with Polaroid, respectively. The photon detection rate results presented in (b), (d) correspond to all axial positions. Similarly, the results presented in (a), (c) correspond to all distances between scintillation points and SiPMs.

(100%) for the detector without Polaroid, 95% of the optical photons were detected by the SiPMs, with 65% of them used for positioning. In the detector with Polaroid, only 75% of all the optical photons were actually absorbed by the SiPMs, with 66% of them used for positioning. Hence, the 66% and 65% refer to the percentage of optical photons used for positioning out of the total number of produced optical photons, not out of those detected by the SiPMs. The rejected photons were those filtered by the positioning threshold ( $\sim 5\%$  – those that were not in the close neighborhood) and the Polaroid ( $\sim 20\%$ ). Although the level of detected photons (blue line) for detectors without Polaroid was much higher than the detector with Polaroid, the ratio of photons used for positioning was approximately the same.

The DOI's FWHM as a function of scintillation point at depths of 2, 4, 6, and 8 mm were estimated and reported in table 3. The role of Polaroid-PET is more evidenced at relatively far distances from SiPMs than close distances.

Figures 6 and 7 illustrate images of the grids along with horizontal intensity profiles drawn on the images of sources for detector modules without and with Polaroid, respectively.

**Table 3.** Depth of interaction resolution for one module with and without Polaroid.

| Depth (mm) | Without Polaroid (mm) | With Polaroid (mm) |
|------------|-----------------------|--------------------|
| 2          | 0.58                  | 0.49               |
| 4          | 0.73                  | 0.56               |
| 6          | 0.94                  | 0.78               |
| 8          | 1.09                  | 0.91               |
| 10         | 1.32                  | 1.06               |

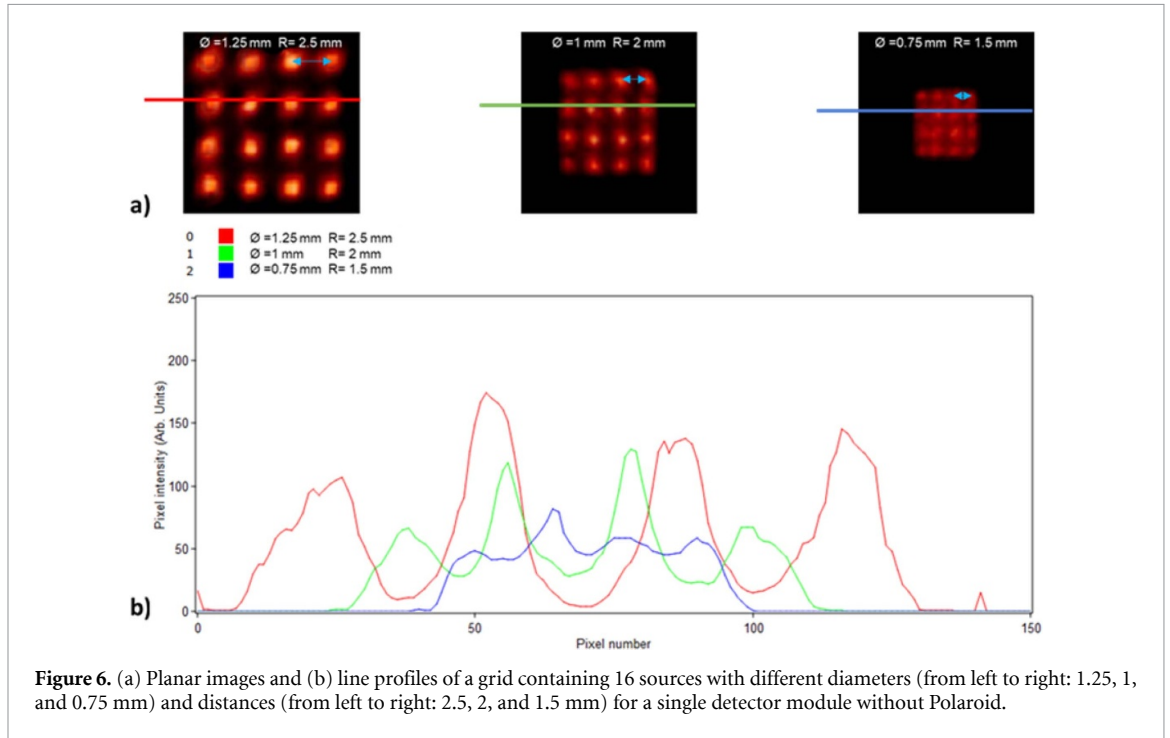


**Figure 6.** (a) Planar images and (b) line profiles of a grid containing 16 sources with different diameters (from left to right: 1.25, 1, and 0.75 mm) and distances (from left to right: 2.5, 2, and 1.5 mm) for a single detector module without Polaroid.

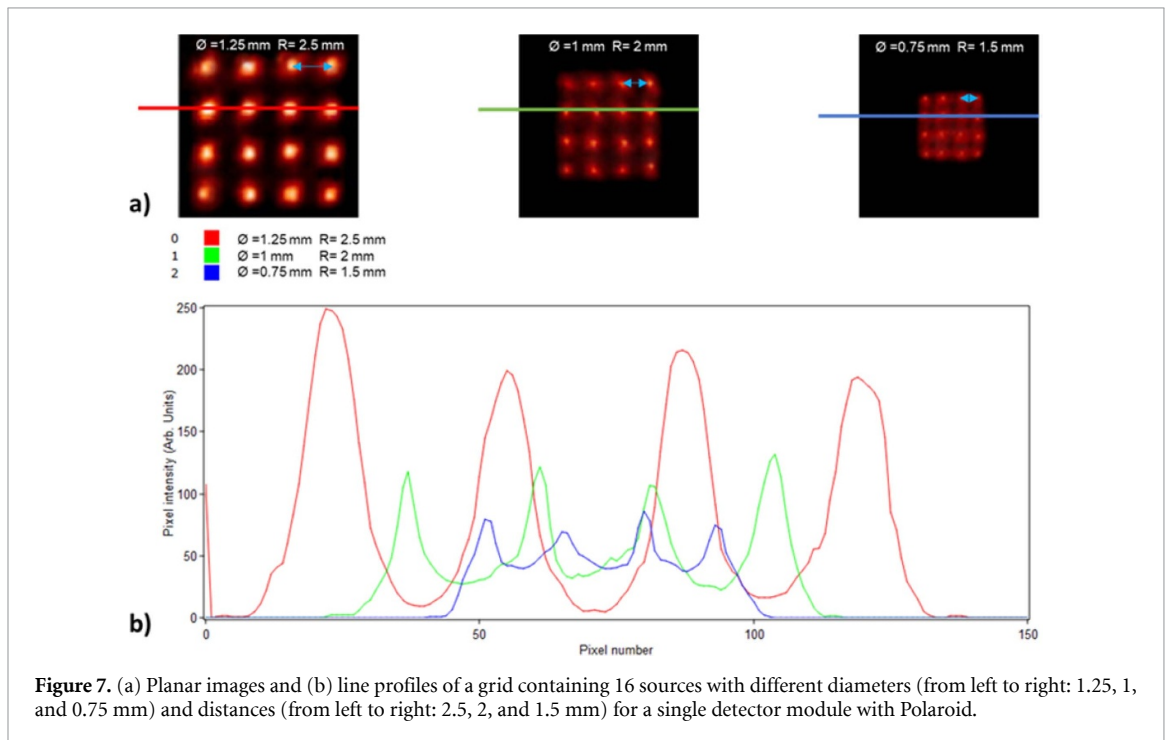


**Figure 7.** (a) Planar images and (b) line profiles of a grid containing 16 sources with different diameters (from left to right: 1.25, 1, and 0.75 mm) and distances (from left to right: 2.5, 2, and 1.5 mm) for a single detector module with Polaroid.

#### 4. Discussion

The plea for further enhancement of key performance parameters of both clinical and preclinical PET scanners, in particular spatial resolution and sensitivity, is one of the main incentives driving the research in

PET instrumentation pursued by a number of research groups in academic and corporate settings. A high spatial resolution and high sensitivity are among the desired performance characteristics acclaimed by the molecular imaging community. A high absolute sensitivity makes it possible to shorten the scanning time and/or lower the injected activity, as well as realizing the intrinsic spatial resolution characteristics of PET. In this work, we proposed a novel PET detector module equipped with a monolithic scintillator and a thin layer of linear Polaroid. The monolithic crystal is intended to enhance/maintain the detection efficiency while the Polaroid would compensate for the spatial resolution loss caused by the reflection and spread of optical photons. This novel PET detector module aims to achieve an improved trade-off between detection efficiency and spatial resolution.

Accurate localization of the interaction point inside the crystal is a prerequisite for reliable restitution of the tracer biodistribution using PET. Straight optical photons originating from exactly the scintillation point carry true and precise information about the event interaction. Conversely, reflected photons originating from the reflector are warped toward the crystal, providing false information about the origin of the scintillation. When these photons reach the SiPMs, they cause glare and haze. Hence, in the ideal case, it is desirable to minimize the effect of reflected photons in positioning and use mostly straight photons. The reflected photon has vertical polarization that can be blocked by a horizontal Polaroid.

For a single detector module fitted with Polaroid, the spatial resolution (FWHM) varies from 1.07 mm at the center to 1.19 mm at the corner of the detector. Conversely, the FWHM for a regular scanner without Polaroid varies between 1.30 mm and 1.39 mm. A possible explanation for the improved spatial resolution at the corner of the detector is the level of reflection and the poor performance of the positioning algorithm at the corner where the Gaussian shape of the light distribution may be severely distorted.

Our results demonstrate that adding a thin layer of Polaroid between LYSO crystals and SiPMs in detector modules improves the spatial resolution by around 18%, while the absolute sensitivity decreases slightly (by ~1.4%) in Polaroid-PET in comparison with regular PET. The results suggest that the change in sensitivity is not the outcome of using the Polaroid because it only plays a role for optical photons, not annihilated photons. The goal of this study is not to present a PET scanner with comparable or better performance than state-of-the-art commercial scanners, but rather to present a method enabling the improvement of the spatial resolution of an existing PET scanner equipped with a monolithic crystal without degrading the sensitivity, through reasonable modification of the hardware that can be accommodated by vendors and academic groups (adding a Polaroid).

An important aspect of this Polaroid-PET scanner design is the way in which scintillation photon transport can be exploited to gain information about event position in the detector. This is the motivation behind carrying out a detailed study of the characteristics of photon transport. In the monolithic crystal, it may be possible for scintillation photons to travel relatively long distances from the scintillation point, potentially making event positioning difficult. Therefore, we studied the fraction of photons that were not detected by the SiPM arrays used in our position calculations. The results indicated that 88% and 95% of the optical photons are detected by SiPMs at the CFOV for the scanner with and without the Polaroid. The residues are not detected, mostly due to the dead zone between the SiPMs' pixels, attenuation in the scintillator and blocking of the optical photons with different polarization by the Polaroid. The plots shown in figures 5(a) and (c) also illustrate that this detection ratio is dependent on the event position, which decreases at the corner the detected photons for the detector module fitted with the Polaroid more than for regular detectors. The reason for decreasing the photon detection ratio at the corners of the detector modules can be attributed to the fact that for scintillation points close to the edge of the crystal the number of reflected photons increases, leading to a change in the polarization and hence blockage by the Polaroid, as a result decreasing the ratio. The widths of the optical photon distributions are a function of the SiPMs' distance, confirming that the width of the photon distribution is related to the depth of the event that can be exploited to estimate the DOI. The DOI resolution for the scanner with and without the Polaroid varies from 0.49 mm and 0.58 mm at 2 mm distance from the SiPMs' surface to 1.06 and 1.32 mm at greater distances (10 mm). For interactions taking place near the SiPMs, the number of straight photons (photons that are not reflected) that reach the SiPMs' pixels is more than the respective number of straight photons reaching the SiPMs for interactions taking place at distances far from the SiPMs' surface.

Since using Polaroid affects the optical photon's summation by the SiPMs, this in turn impacts on the energy resolution, indirectly decreasing the sensitivity. Since the number of optical photons used for positioning and energy discrimination is relatively equal, a deterioration of the above-mentioned parameters is not expected. Yet, this might be an issue in an experimental setting or when a different configuration is considered.

The qualitative assessment illustrates the potential advantages of high-resolution imaging using Polaroid-PET. Specifically, the 1.25 mm and 1 mm diameter spheres are discernible from their neighbors on both scanners, while the 0.75 mm diameter spheres appear to be clearly discernible only on the Polaroid-PET

and difficult to depict on the regular PET (figures 6 and 7). These visual assessments are supported by the intensity profiles drawn on the images.

One of the limitations of this work is the lack of experimental validation of the proposed approach. Experimental validation requires careful planning and access to instruments and components. Further investigation along these lines is guaranteed. Another limitation was the computational burden associated with the simulation of optical photon transport, which limited the performance assessment to key performance parameters, hence discarding the assessment of image quality. Moreover, the lack of evaluation and comparison of energy resolution for both configurations, a parameter with a relevant impact on the rejection of Compton scattered events, is another limitation of this work.

## 5. Conclusion

A novel design of a preclinical PET detector module/scanner based on monolithic crystals and Polaroid was introduced to concurrently improve the spatial resolution and detection sensitivity. The underlying concept consisted of using a thin layer of polarized film between monolithic LYSO crystals and SiPMs. The monolithic crystal, having intrinsically higher sensitivity, retains/enhances the detection efficiency of the scanner. Conversely, the Polaroid enables the detectors to remove multi-reflected optical photons, thus leading to higher spatial resolution. This novel design may improve the trade-off between sensitivity and spatial resolution, resulting in a spatial resolution of 0.83 mm and a sensitivity of 4.31% at the CFOV of the considered preclinical PET scanner.

## Acknowledgments

This work was supported by the Swiss National Science Foundation under grant SNFN 320030-176052, the Eurostars programme of the European commission under grant E! 114021 ProVision and the Private Foundation of Geneva University Hospitals under Grant RC-06-01.

## ORCID iDs

Amirhossein Sanaat  <https://orcid.org/0000-0001-8437-2060>

Habib Zaidi  <https://orcid.org/0000-0001-7559-5297>

## References

- Agostinelli S et al 2003 GEANT4—a simulation toolkit *Nucl. Instrum. Methods Phys. Res. A* **506** 250–303
- Allison J et al 2006 Geant4 developments and applications *IEEE Trans. Nucl. Sci.* **53** 270–8
- Allison J et al 2016 Recent developments in Geant4 *Nucl. Instrum. Methods Phys. Res. A* **835** 186–225
- Amirrahshedi M, Sarkar S, Ghafarian P, Shahraki R H, Geramifar P, Zaidi H and Ay M R 2019 NEMA NU-4 2008 performance evaluation of Xtrim-PET: a prototype SiPM-based preclinical scanner *Med. Phys.* **46** 4816–25
- Andreou A G and Kalayjian Z K 2002 Polarization imaging: principles and integrated polarimeters *IEEE Sens. J.* **2** 566–76
- Berg E and Cherry S R 2018 Innovations in instrumentation for positron emission tomography *Semin. Nucl. Med.* **48** 311–31
- Blackberg L, Moebius M, Fakhri G E, Mazur E and Sabet H 2018 Light spread manipulation in scintillators using laser induced optical barriers *IEEE Trans. Nucl. Sci.* **65** 2208–15
- Brun R and Rademakers F 1997 ROOT—an object oriented data analysis framework *Nucl. Instrum. Methods Phys. Res. A* **389** 81–6
- Cherry S R et al 1997 MicroPET: a high resolution PET scanner for imaging small animals *IEEE Trans. Nucl. Sci.* **44** 1161–6
- Collett E 2005 *Field Guide to Polarization* (Bellingham, WA: SPIE Press)
- De Paola G 2003 New Monte Carlo method for Compton and Rayleigh scattering by polarized gamma rays *Nucl. Instrum. Methods Phys. Res. A* **512** 619–30
- Flower M 2012 *Webb's Physics of Medical Imaging* (Boca Raton, FL: CRC Press)
- Galasso M, Fabbri A, Borrazzo C, Cencelli V O and Pani R 2016 A theoretical model for fast evaluation of position linearity and spatial resolution in gamma cameras based on monolithic scintillators *IEEE Trans. Nucl. Sci.* **63** 1386–98
- Ghabrial A, Franklin D and Zaidi H 2018 A Monte Carlo simulation study of the impact of novel scintillation crystals on performance characteristics of PET scanners *Phys. Med.* **50** 37–45
- Godinez F, Chaudhari A J, Yang Y, Farrell R and Badawi R D 2012 Characterization of a high-resolution hybrid DOI detector for a dedicated breast PET/CT scanner *Phys. Med. Biol.* **57** 3435–45
- Ikeuchi K 2014 *Computer Vision: A Reference Guide* (New York: Springer)
- Iqbal M 2011 Polarization stereoscopic imaging prototype *Ph.D Thesis* Université de Bourgogne, Dijon
- Jansen F P and Binnie D M 1996 Signal processing in scintillation cameras for nuclear medicine *US Patent Specification* US5504334A
- Jones T and Townsend D W 2017 History and future technical innovation in positron emission tomography *J. Med. Imaging* **4** 011013
- Können G 1985 *Polarized Light in Nature* (Cambridge: Cambridge University Press)
- Labella A, Cao X, Petersen E, Lubinsky R, Biegon A, Zhao W and Goldan A H 2020 High resolution depth-encoding PET detector module with prismatic light guide array *J. Nucl. Med.* (accepted) (<https://doi.org/10.2967/jnumed.119.239343>)
- Levin A and Moisan C A 1996 More physical approach to model the surface treatment of scintillation counters and its implementation into DETECT *IEEE Nuclear Science Symp. Conf. Record* (2–9 November) pp 702–6
- Lewellen T K 2010 The challenge of detector designs for PET *Am. J. Roentgenol.* **195** 301–9

- Maas M C, Schaart D R, van der Laan D J, Bruyndonckx P, Lemaitre C, Beekman F J and van Eijk C W 2009 Monolithic scintillator PET detectors with intrinsic depth-of-interaction correction *Phys. Med. Biol.* **54** 1893–908
- Miyaoka R and Lewellen T 2000 Effect of detector scatter on the decoding accuracy of a DOI detector module *IEEE Trans. Nucl. Sci.* **47** 1614–9
- Moses W W 2011 Fundamental limits of spatial resolution in PET *Nucl. Instrum. Methods Phys. Res. A* **648** S236–S40
- Moses W W 2001 Trends in PET imaging *Nucl. Instrum. Methods Phys. Res.* **471** 209–14
- National Electrical Manufacturers Association 2008 NEMA Standards publication NU 4-2008. Performance measurements of small animal positron emission tomographs (Rosslyn, VA: National Electrical Manufacturers Association)
- Nayar S K, Ikeuchi K and Kanade T 1991 Surface reflection: physical and geometrical perspectives *IEEE Trans. Pattern Anal. Mach. Intell.* **13** 611–34
- Ota R, Omura T, Yamada R, Miwa T and Watanabe M 2016 Evaluation of a sub-millimeter resolution PET detector with a 1.2 mm pitch TSV-MPPC array one-to-one coupled to LFS scintillator crystals and inter-crystal scatter studies with individual signal readout *IEEE Trans. Radiat. Plasma Med. Sci.* **1** 15–22
- Peatross J and Ware M 2017 *Physics of Light and Optics* vol 3 (Provo, UT: Brigham Young University, Department of Physics)
- Pedrotti F L, Pedrotti L M and Pedrotti L S 2017 *Introduction to Optics* (Cambridge: Cambridge University Press)
- Pierce L, Pedemonte S, Dewitt D, Macdonald L, Hunter W, Van Leemput K and Miyaoka R 2018 Characterization of highly multiplexed monolithic PET/gamma camera detector modules *Phys. Med. Biol.* **63** 075017
- Ramirez R A, Liu S, Liu J, Zhang Y, Kim S, Baghaei H and Wong W-H 2008 High-resolution LYSO detectors using PMT-quadrant-sharing for human and animal PET cameras *IEEE Trans. Nucl. Sci.* **55** 862–9
- Sabet H, Kudrolli H, Singh B and Nagarkar V V 2012 Fabricating high-resolution and high-sensitivity scintillator arrays using Laser Induced Optical Barriers *IEEE Nuclear Science Symp. and Medical Imaging Conf. Record* pp 4080–4
- Sajedi S, Zeraatkar N, Taheri M, Kaviani S, Khanmohammadi H, Sarkar S, Sabet H and Ay M R 2019 Development and preliminary results of Xtrim-PET, a modular cost-effective preclinical scanner *Nucl. Instrum. Methods Phys. Res. A* **940** 288–95
- Sanaat A, Arabi H, Ay M R and Zaidi H 2020 Novel preclinical PET geometrical concept using a monolithic scintillator crystal offering concurrent enhancement in spatial resolution and detection sensitivity: a simulation study *Phys. Med. Biol.* **65** 045013
- Sanaat A, Ay M R, Farahani M H and Sarkar S 2019a Altering paths of optical photons passing through a scintillator *US Patent Specification* US20190361132A1
- Sanaat A, Zafarhandi M S and Ay M R 2019b Design and performance evaluation of high resolution small animal PET scanner based on monolithic crystal: a simulation study *J. Instrum.* **14** P01005-P
- Sanaat A and Zaidi H 2019 Accurate estimation of depth of interaction in PET on monolithic crystal coupled to SiPMs using a deep neural network and Monte Carlo simulations *IEEE Nuclear Science Symp. and Medical Imaging Conf. (NSS/MIC)* pp 1–3
- Sanaat A and Zaidi H 2020 Depth of interaction estimation in a preclinical PET scanner equipped with monolithic crystals coupled to SiPMs using a deep neural network *Appl. Sci.* **10** 4753
- Seifert S, Van der Lei G, Van Dam H T and Schaart D R 2013 First characterization of a digital SiPM based time-of-flight PET detector with 1 mm spatial resolution *Phys. Med. Biol.* **58** 3061
- Surti S, Pantel A R and Karp J S 2020 Total body PET: why, how, what for? *IEEE Trans. Radiat. Plasma Med. Sci.* **4** 283–92
- Teimourian Fard B and Shamsaei Zafarhandi M 2019 Comparative assessment of the accuracy of maximum likelihood and correlated signal enhancement algorithm positioning methods in gamma camera with large square photomultiplier tubes *Iran. J. Nucl. Med.* **27** 81–6
- Thielemans K, Tsoumpas C, Mustafovic S, Beisel T, Aguiar P, Dikaios N and Jacobson M W 2012 STIR: software for tomographic image reconstruction release 2 *Phys. Med. Biol.* **57** 867–83
- Van der Laan D J, Schaart D R, Maas M C, Beekman F J, Bruyndonckx P and van Eijk C W 2010 Optical simulation of monolithic scintillator detectors using GATE/GEANT4 *Phys. Med. Biol.* **55** 1659–75
- Van Sluis J, de Jong J, Schaar J, Noordzij W, van Snick P, Dierckx R, Borra R, Willemsen A and Boellaard R 2019 Performance characteristics of the digital biograph vision PET/CT system *J. Nucl. Med.* **60** 1031–6
- Vinke R, van Dam H T, Seifert S, Beekman F J, Löhner H, Schaart D R and Dendooven P 2010 Thick monolithic scintillation crystals for TOF-PET with depth-of-interaction measurement *IEEE Nuclear Science Symp. and Medical Imaging Conf. (Knoxville, TN, USA)* pp 1981–4
- Zaidi H 2014 *Molecular Imaging of Small Animals: Instrumentation and Applications* (Berlin: Springer)
- Zaidi H and Karakatsanis N 2017 Towards enhanced PET quantification in clinical oncology *Br. J. Radiol.* **91** 20170508
- Zein S A, Karakatsanis N A, Issa M, Haj-Ali A A and Nehmeh S A 2020 Physical performance of a long axial field-of-view PET scanner prototype with sparse rings configuration: a Monte Carlo simulation study *Med. Phys.* **47** 1949–57
- Zeraatkar N, Sajedi S, Fard B T, Kaviani S, Akbarzadeh A, Farahani M, Sarkar S and Ay M R 2017 Development and calibration of a new gamma camera detector using large square photomultiplier tubes *J. Instrum.* **12** P09008
- Zhang X, Cherry S R, Xie Z, Shi H, Badawi R D and Qi J 2020 Subsecond total-body imaging using ultrasensitive positron emission tomography *Proc. Natl. Acad. Sci. USA* **117** 2265–7